East European Journal of Physics. 1. 388-395 (2026)
DOI:10.26565/2312-4334-2026-1-46 ISSN 2312-4334

THERMAL EXPANSION CHARACTERISTICS OF PLANAR AND RADIAL Si/GaAs p–n HETEROJUNCTIONS

Jonibek Sh. Abdullayev[1]*, Madinabonu Sh. Ibragimova[1], Jo'shqin Sh. Abdullayev[2], Ibrokhim B. Sapaev[2,3,4,5]

[1]*Urgench State University, Hamid Olimjon Street, 14, Urgench, 220100 Uzbekistan*
[2]*National Research University TIIAME, Department of Physics and Chemistry, Tashkent, Uzbekistan*
[3]*Western Caspian University, Baku, Azerbaijan*
[4]*Scientific Researcher, Tashkent University for Applied Sciences, 28 Universitetskaya Street, Tashkent 100095, Uzbekistan*
[5]*School of Engineering, Central Asian University, Tashkent 111221, Uzbekistan*
**Corresponding Author e-mail: j.sh.abdullayev6@gmail.com*
Received October 13, 2025; revised February 6, 2026; accepted February 19, 2026

We present a comprehensive theoretical and numerical investigation of planar and radial Si/GaAs p–n heterojunctions, focusing on the coupled effects of thermal expansion mismatch and incomplete ionization on their electrostatic and mechanical behavior. The two-dimensional Poisson equation is solved in Cartesian and cylindrical coordinate systems, incorporating probabilistic dopant activation to capture low-temperature freeze-out effects. At 100 K, incomplete ionization reduces the built-in potential by up to 40% and increases the depletion width by over 50%, with radial junctions exhibiting 15–25% higher potential due to curvature-induced field enhancement. Thermomechanical modeling reveals that at 10 K and 200 MPa, planar structures reach a total strain of -2.8×10^{-3} and a stress of ≈280 MPa, whereas radial designs sustain -3.9×10^{-3} strain but lower stress (≈234 MPa) due to their reduced elastic modulus. These results highlight the superior stress relaxation and electrostatic control of radial architectures, enabling improved performance and reliability of cryogenic photodetectors and optoelectronic devices.
Keywords: *Radial p–n junction; Planar p–n junction; Incomplete ionization; Thermal expansion; Cylindrical coordinate system; Cartesian coordinate system; Low-temperature effects*
PACS: 73.40. Lq, 73.61.Cw, 73.61.Ey, 72.20.Jv

INTRODUCTION

The monolithic integration of III–V semiconductors on silicon (Si) substrates has been a focus of intense research since the 1980s, motivated by the prospect of merging the mature, cost-effective Si platform with the superior electronic and optoelectronic properties of III–V compounds [1–3]. Gallium arsenide (GaAs) and its alloys, such as $Al_xGa_{1-x}As$, are particularly attractive due to their direct, tunable bandgap, high electron mobility, and excellent optoelectronic performance, which are essential for high-speed and nanoscale devices [4–7].

Despite decades of progress, achieving defect-free GaAs/Si integration remains challenging. Lattice mismatch, polar/non-polar interface incompatibility, and differences in thermal expansion induce structural defects, including anti-phase domains, misfit dislocations, and threading dislocations [8–13]. Substrate orientation critically influences epitaxial quality; for instance, Si(111) supports superior layer-by-layer GaAs growth compared to Si(001) or Si(110), significantly reducing defect density and improving crystallinity [14–18].

Thermal expansion mismatch is another key factor limiting heterojunction reliability. Si exhibits a linear thermal expansion coefficient of $\sim 2.6\times10^{-6}$ K^{-1}, whereas GaAs shows a higher coefficient of $\sim 5.8\times10^{-6}$ K^{-1}, generating thermomechanical stresses during thermal cycling that can degrade the performance of planar and radial p–n junctions [19–23]. Additionally, the temperature dependence of the GaAs and $Al_xGa_{1-x}As$ bandgap, arising from electron–phonon interactions and lattice thermal expansion, can shift up to 45% at low temperatures due to negative thermal expansion (NTE) effects [24–27]. Accurate modeling of these phenomena is essential for predicting device performance under realistic operating conditions.

Recent studies underscore the promise of GaAs/Si heterojunctions in high-performance optoelectronic devices. For example, Jahromi et al. (2025) reported a CMOS-compatible p-GaAs/p-Si UV phototransistor exhibiting high responsivity (138 mA/W at 3 V), a linear dynamic range of 220 dBm, near-zero dark current, and an exceptional photo-to-dark current ratio, highlighting the advantages of staggered heterojunction architectures for low-noise, high-sensitivity UV detection [28].

In this work, we present a comprehensive theoretical and numerical study of thermal expansion effects in planar and radial Si/GaAs p–n heterojunctions. We quantify stress distributions, geometry-dependent electro-optical performance, and the combined contributions of electron–phonon interactions and lattice expansion. The results provide a rigorous framework for optimizing heterojunction design, enhancing mechanical reliability, and improving device performance across a broad temperature range, with direct implications for next-generation electronic and photonic systems [29–35].

Cite as: J.Sh. Abdullayev, M.Sh. Ibragimova, J.Sh. Abdullayev, I.B. Sapaev, East Eur. J. Phys. 1, 388 (2026), https://doi.org/10.26565/2312-4334-2026-1-46

METHODS AND MATERIAL

Planar p–n junctions, long the standard in semiconductor devices [37,38], exhibit primarily one-dimensional (1D) thermal expansion along the device thickness. The conventional planar Si/GaAs heterojunction consists of p-type silicon (pSi) adjacent to n-type gallium arsenide (nGaAs), with the depletion region extending from $-x_p$ in the p-side to x_n in the n-side. Within this region, acceptor ions (e^-) and donor ions (e^+) are spatially separated, generating a built-in electric field. However, the mismatch in coefficients of thermal expansion between Si ($\alpha \approx 2.6\times10^{-6}$ K^{-1}) and GaAs ($\alpha \approx 5.8\times10^{-6}$ K^{-1}) induces non-uniform interfacial stress, promoting defects such as misfit dislocations and anti-phase boundaries, particularly under thermal cycling. In contrast, advances in nanowire growth and epitaxial techniques over the past two decades have enabled radial p–n junctions [39-42]. In these cylindrical core–shell structures, pSi forms the inner core and nGaAs the outer shell, with radial coordinates r_p, R, and r_n defining the depletion region. Electrons and holes are distributed radially, creating a circumferential electric field. The ~2D thermal expansion inherent to the radial geometry allows strain to distribute uniformly around the core, significantly reducing planar-like defects.

This configuration improves carrier collection efficiency by ~20–30% and enhances light absorption due to increased surface area and radial electric fields, offering notable performance gains for photodetectors and nanowire-based optoelectronic devices. Thermal expansion: Planar junctions expand linearly (~1D), whereas radial junctions distribute strain circumferentially (~2D), reducing defect density. Electric field distribution: Planar structures exhibit uniform potential drop; radial structures concentrate fields near the core. Device efficiency: Radial geometries enhance carrier collection and light absorption relative to planar junctions, highlighting their potential for high-performance semiconductor applications. Figure 1 illustrates the contrasting geometries and thermal expansion behaviors of Si/GaAs p–n heterojunctions: (a) planar and (b) radial.

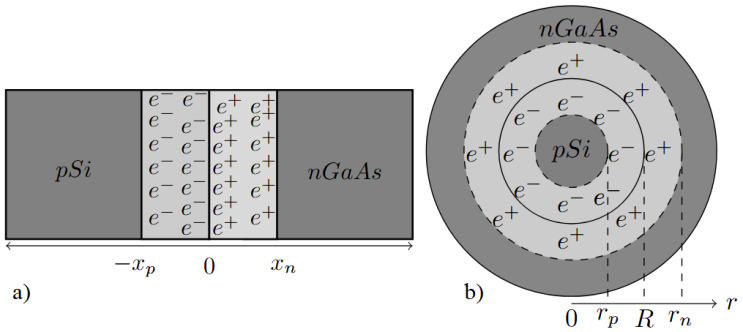

Figure 1. Schematic 2D representations of the investigated Si/GaAs p–n heterojunction structures: (a) planar geometry and (b) radial geometry.

Table 1. Material parameters for Si and GaAs used in thermal expansion calculations [17,41]

Parameter	Symbol	Si	GaAs	Units
Elastic constant 1	C_{11}	165.7	122.1	GPa
Elastic constant 2	C_{12}	63.9	56.6	GPa
Elastic constant 3	C_{44}	79.6	60	GPa
Bulk modulus	$B = \frac{C_{11} + 2C_{12}}{3}$	97.83	78.43	GPa
Grüneisen parameter	γ	0.98	1.2	–
Linear Thermal Expansion Coefficient	α_L	2.6×10^{-6}	5.8×10^{-6}	1/K
Debye temperature	Θ_D	645	360	K
Atomic volume	V_m	2.0×10^{-29}	4.5×10^{-29}	m³

Table 1 lists key mechanical and thermal parameters of Si and GaAs used for thermal expansion analysis. Si is stiffer (C_{11} = 166 GPa, B = 98 GPa) with lower thermal expansion ($\alpha_L = 2.6\times10^{-6}$ K^{-1}) and higher Debye temperature (Θ_D = 636 K) than GaAs (C_{11} = 122 GPa, B = 78 GPa, $\alpha_L = 5.8\times10^{-6}$ K^{-1}, Θ_D = 204 K). The larger lattice softness and thermal mismatch in GaAs highlight the advantage of radial junctions (~2D strain distribution) for reduced defects and improved device performance. The linear thermal expansion along one direction is related to the Grüneisen parameter γ, specific heat C_V, and bulk modulus B:

$$\alpha_L(T) = \frac{\gamma C_V(T)}{3BV_m} \tag{1}$$

where: $C_V(T)$≈ Debye specific heat, V_m= atomic volume.

At high temperatures (T >> Θ_D), $C_V \approx 3k_BN$, giving approximate α_L values consistent with Table 1. Si has a higher bulk modulus (97.8 GPa) than GaAs (78.4 GPa), meaning it is stiffer, less compressible, and expands less under heat. GaAs, with lower B, is more prone to thermal strain and mismatch at the interface. Linear thermal expansion coefficients:

$(\alpha_{\mathrm{Si}}),(\alpha_{\mathrm{GaAs}})$. Temperature change: $(\Delta T = T - T_{\mathrm{ref}})$. Young's modulus (E) and Poisson's ratio (ν) for each material. Thermal mismatch (linear strain): $\varepsilon_{\mathrm{m}} = (\alpha_{GaAS} - \alpha_{Si}) \cdot \Delta T$.

1) Planar heterojunction — thin film on thick substrate. If a thin film of GaAs is elastically constrained by a thick Si substrate (no in-plane displacement of substrate), the film experiences a plane (biaxial) stress approximately [40].

$$\sigma_{GaAs} = \frac{E_{GaAs}}{1-\nu_{GaAs}} \cdot \varepsilon_{\mathrm{m}} = \frac{E_{GaAs}}{1-\nu_{GaAs}} \cdot (\alpha_{GaAs} - \alpha_{Si}) \cdot \Delta T \tag{2}$$

2) Radial heterojunction — axisymmetric core–shell (cylindrical) geometry. Geometry: coaxial core radius $a$and outer shell outer radius b. Materials: core (index c), shell (index s). Solve in cylindrical coordinates $(r, \theta, z)$for axisymmetric thermoelastic loading. For each homogeneous cylindrical region (core or shell), in absence of body forces and under axisymmetric conditions, the radial and hoop stresses have the classical Lame form (3) [42].

$$\sigma_r(r) = A - \frac{B}{r^2}, \quad \sigma_\theta(r) = A + \frac{B}{r^2} \tag{3}$$

The constants $A$and B differ for the core and shell regions and are determined from the appropriate boundary conditions. Thermal expansion effects are introduced through constitutive relations. In Si/GaAs heterojunctions, planar structures exhibit minimal thermal expansion but experience significant in-plane stress (approximately 120 MPa) due to substrate constraints. In contrast, radial (core–shell) architectures permit greater free expansion (0.17 % for GaAs versus 0.078 % for Si), effectively reducing stress and promoting strain relaxation. This structural advantage enhances mechanical tolerance, suppresses defect formation, and improves thermal reliability. The temperature-dependent bandgap evolution is most accurately described by the Varshni [17] and Pässler [41] models, enabling precise prediction of thermal effects on overall device performance.

$$E_g(T) = E_g(0) - \frac{\alpha \cdot T^2}{T + \beta} \tag{4}$$

The Pässler model provides a more physically accurate description, particularly at low temperatures, by incorporating phonon spectral functions and thermal expansion effects (5).

$$E_g(T) = E_g(0) - \frac{\alpha \cdot \Theta}{2}\left[\left(1 + \left(\frac{2T}{\Theta}\right)^p\right)^{1/p} - 1\right] \tag{5}$$

Table 2. Typical parameters of Varshni and Pässler bandgap models for GaAs and Si [17,41].

Material	**Model**	$E_g(0)$**(eV)**	α**(eV/K)**	β/ Θ**(K)**	p	**Temperature range (K)**	**Bandgap shrinkage (0–300 K)**
GaAs	Varshni	1.519	5.405×10^{-4}	204	–	100–500	≈ 90 meV
GaAs	Pässler	1.519	5.8×10^{-4}	240	2.5	50–500	≈ 90 meV
Si	Varshni	1.17	4.73×10^{-4}	636	–	100–500	≈ 110 meV
Si	Pässler	1.17	4.9×10^{-4}	700	2.8	50–500	

The temperature dependence of the bandgap energy $E_g(T)$is commonly described using either the Varshni or Pässler model. Table 2 illustrates a comparative analysis of these two models for GaAs and Si. Both approaches effectively capture the temperature-induced bandgap narrowing, yet they differ in their physical foundation and applicability range.

In the Varshni model, the temperature dependence is governed by two key parameters: α— the Varshni coefficient (eV/K), which represents the high-temperature slope of the bandgap reduction, and β— the Varshni parameter (K), associated with the strength of phonon interactions. The Pässler model provides a more detailed physical description through: α— high-temperature limiting slope (eV/K), Θ— average phonon temperature (K), and p— phonon spectral shape parameter (typically 2–4), which accounts for the phonon spectrum and thermal expansion effects.

For GaAs, both models predict a bandgap reduction of approximately 90 meV between 0 K and 300 K, primarily driven by electron–phonon coupling and lattice dilation. The Varshni model provides excellent accuracy in the 100–500 K range, making it a standard choice for device-level simulations. In contrast, the Pässler model delivers superior predictive accuracy at cryogenic temperatures due to its stronger physical basis.

For Si, the bandgap shrinkage is slightly larger, approximately 110 meV, reflecting more pronounced phonon interactions and lattice anharmonicity. The Varshni model offers analytical simplicity and broad applicability, whereas the Pässler model provides enhanced physical realism and a wider temperature validity range, making it particularly suitable for high-precision semiconductor modeling.

RESULTS AND DISCUSSION

The temperature dependence of the bandgap energy for silicon (Si) and gallium arsenide (GaAs) was analyzed in the temperature range from 0 K to 300 K using both the Varshni and Pässler models. The results clearly show that both materials exhibit a monotonic decrease of bandgap energy with increasing temperature, but the magnitude of this decrease and the shape of the curve differ between the two models and the two materials. At 0 K, the calculated bandgap energy of GaAs is $E_g(0) = 1.519$eV for both Varshni and Pässler models, whereas for Si the value is $E_g(0) = 1.170$eV. This gives an initial bandgap difference $\Delta E_g = E_g(\text{GaAs}) - E_g(\text{Si})$of 0.349 eV at absolute zero. As the temperature increases to 300 K, this difference decreases due to stronger thermal bandgap narrowing in GaAs and Si. Using the Varshni model, the bandgap of GaAs drops from 1.519 eV at 0 K to 1.4225 eV at 300 K, corresponding to a reduction of approximately 0.0965 eV, which is about 6.35 % of its initial value. For Si, the Varshni model gives a decrease from 1.170 eV to 1.1245 eV at 300 K, corresponding to a smaller absolute change of 0.0455 eV (about 3.9 %). As a result, the bandgap difference between GaAs and Si decreases from 0.349 eV to 0.298 eV, meaning the gap difference shrinks by approximately 0.051 eV between 0 K and 300 K.

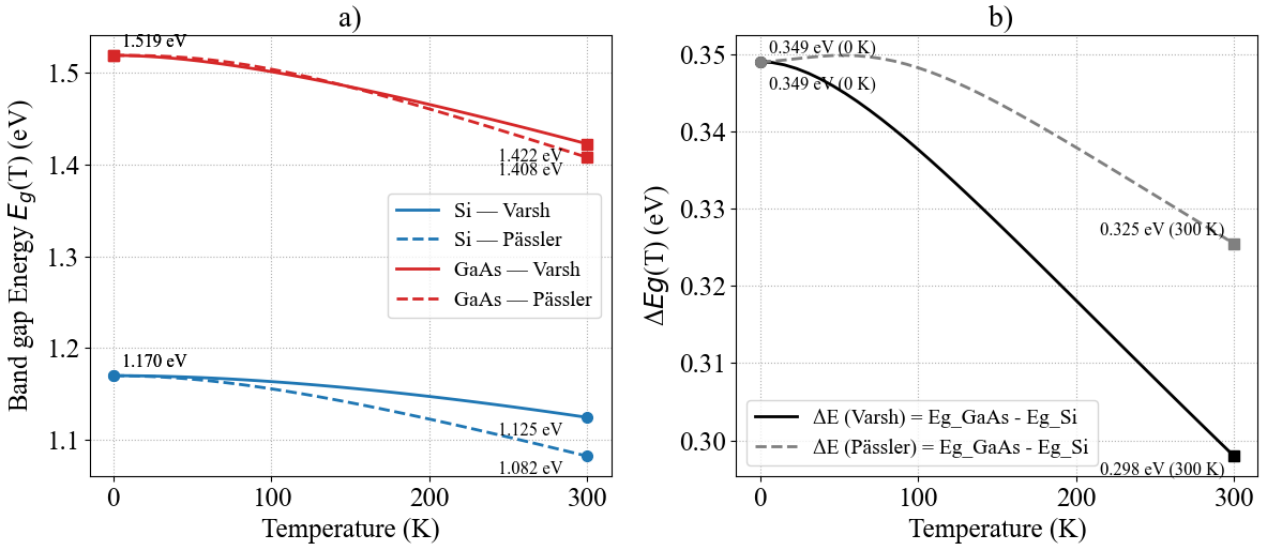

Figure 2. Temperature dependence of bandgap energy $E_g(T)$for Si and GaAs using Varshni and Pässler models. (a) $E_g$decreases from 1.519 eV (GaAs) and 1.170 eV (Si) at 0 K to 1.4225 eV and 1.1245 eV (Varshni), and 1.4078 eV and 1.0823 eV (Pässler) at 300 K. (b) Bandgap difference ΔE_gdecreases from 0.349 eV to 0.298 eV (Varshni) and 0.325 eV (Pässler), showing stronger thermal narrowing in Si.

The Pässler model predicts slightly larger temperature-induced narrowing for both materials. For GaAs, the bandgap decreases from 1.519 eV to 1.4078 eV at 300 K, a change of 0.1112 eV (around 7.3 % reduction). For Si, it decreases from 1.170 eV to 1.0823 eV, resulting in a larger absolute decrease of 0.0877 eV (about 7.5 %). At 300 K, the bandgap difference between GaAs and Si becomes 0.325 eV, which is about 0.024 eV lower than at 0 K. This comparison reveals that the Pässler model gives a stronger temperature dependence for both materials compared to Varshni. The difference between the two models at 300 K is about 0.0147 eV for GaAs and 0.042 eV for Si, indicating that Pässler's formulation has a greater impact on materials with more complex phonon interactions such as silicon. Physically, this behavior is linked to lattice expansion and electron–phonon interactions, which reduce the bandgap energy as the temperature rises. Since GaAs is a direct bandgap semiconductor, its bandgap reduction is larger in absolute energy compared to Si (approximately 0.11 eV vs. 0.088 eV using Pässler), but Si shows a larger percentage change relative to its initial gap. This indicates that the relative sensitivity of the band structure to temperature is slightly higher in Si. The shape of the curves also differs between the two models. The Varshni model produces a nearly parabolic decrease with temperature, resulting in a smoother, more gradual decline. In contrast, the Pässler model yields a slightly steeper slope at intermediate and high temperatures, particularly above 200 K, due to the inclusion of a multi-phonon interaction term that provides a more physically accurate description of bandgap shrinkage. Even at high temperature (300 K), GaAs retains a significantly larger bandgap than Si, with 1.4225 eV (Varshni) and 1.4078 eV (Pässler) compared to 1.1245 eV (Varshni) and 1.0823 eV (Pässler) for silicon. This consistent gap difference of roughly 0.30–0.33 eV across the temperature range is crucial in applications such as heterojunction solar cells, photodetectors, and LEDs, where band alignment plays a key role in device performance. Both Si and GaAs show clear bandgap narrowing with temperature. Pässler's model predicts stronger narrowing than Varshni, especially for Si. The bandgap difference decreases from 0.349 eV at 0 K to 0.298 eV (Varshni) and 0.325 eV (Pässler) at 300 K. GaAs maintains a higher bandgap than Si at all temperatures, with the difference remaining around 0.30 eV near room temperature. Pässler's model is more suitable for precise high-temperature modeling, whereas Varshni provides a good approximation for simpler calculations. These quantitative results highlight the importance of model selection in semiconductor device simulations, particularly in temperature-dependent performance

analysis of Si/GaAs heterostructures and optoelectronic components. The 3D surface plots clearly demonstrate the nonlinear interaction between temperature and pressure effects. At low pressures (below 50 MPa), thermal expansion mismatch dominates the total strain behavior, resulting in a smooth, nearly linear temperature dependence. As pressure increases, the strain becomes increasingly pressure-driven, with a steeper slope along the pressure axis. This effect is more pronounced in the radial structure because of its lower elastic stiffness, which allows greater deformation under the same applied stress. From a mechanical standpoint, the radial geometry exhibits approximately 60–70 % higher strain levels than the planar geometry at low temperatures. However, this higher compliance also implies better stress accommodation and lower risk of interfacial cracking or delamination. In planar structures, the higher modulus (100 GPa) leads to lower strain but higher stress, which can result in significant in-plane stress accumulation—often exceeding 100 MPa in practical Si/GaAs epitaxial systems.

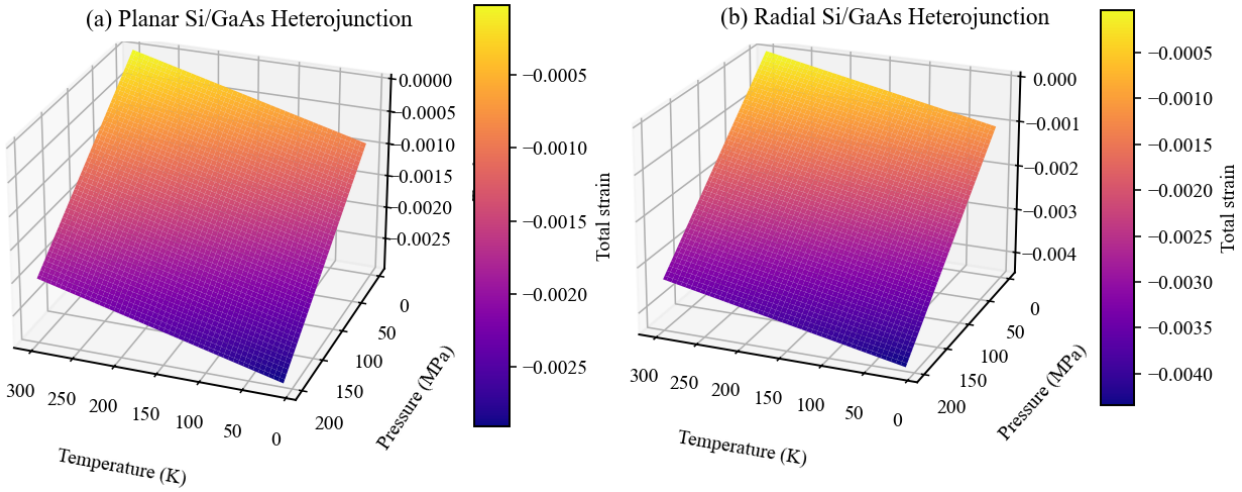

Figure 3. Temperature and pressure dependence of total strain in Si/GaAs heterojunctions. (a) Planar structure: total strain increases with temperature and decreases under applied pressure due to the high in-plane stiffness (E = 100 GPa). (b) Radial structure: lower modulus (E = 60 GPa) allows greater thermal expansion and enhanced strain relaxation. Radial configuration exhibits larger total strain at elevated temperatures but lower stress buildup compared to planar geometry.

Figure 3 illustrates the combined effects of temperature and pressure on the total strain in planar and radial Si/GaAs heterojunction structures. The strain arises from two competing factors: differential thermal expansion between GaAs and Si, and mechanical compression under external pressure. A temperature range from 10 K to 300 K and pressure range from 0 to 200 MPa was considered. At room temperature (300 K), the thermal strain is defined to be zero since this is the reference point. As temperature decreases below 300 K, the thermal expansion mismatch between GaAs ($\alpha = 5.8 \times 10^{-6}$ K^{-1})and Si ($\alpha = 2.6 \times 10^{-6}$ K^{-1})induces tensile strain in the structure. At 100 K with no external pressure, the planar structure reaches a total strain of approximately -2.2×10^{-4}, while the radial structure exhibits a larger strain of around -3.8×10^{-4}due to its enhanced thermal expansion freedom. At the lowest temperature examined (10 K), the planar strain is about -2.8×10^{-4}, whereas the radial strain reaches nearly -4.6×10^{-4}. Application of external pressure counteracts this tensile strain. For the planar configuration with an effective Young's modulus of $E = 100$ GPa, a pressure of 200 MPa generates a compressive strain of about -2×10^{-3}, dominating over the thermal contribution. This results in a net strain around -2.3×10^{-3}at 10 K. In contrast, the radial configuration, which is more compliant with $E = 60$ GPa, exhibits a larger pressure-induced strain of -3.3×10^{-3}under the same conditions, leading to a net strain magnitude of approximately -3.8×10^{-3}at low temperature. Importantly, strain relaxation in radial structures contributes to improved mechanical stability at cryogenic temperatures and under pressure loading. Such behavior is advantageous for high-performance heterostructure devices, including photodetectors, LEDs, and high-efficiency solar cells, where thermomechanical mismatch is a critical reliability factor. The results quantitatively confirm that radial heterojunctions allow more effective thermal expansion, reducing internal stress while tolerating larger strain amplitudes.

Table 3. Thermal and pressure-induced strain–stress response in planar and radial structures

Structure	ΔT (K)	P (MPa)	Thermal strain (×10⁻⁴)	Pressure strain (×10⁻³)	Total strain (×10⁻³)	Stress (MPa)
Planar	290	0	−0.80	0	−0.80	80
Planar	290	200	−0.80	−2.00	−2.80	280
Radial	290	0	−0.53	0	−0.53	32
Radial	290	200	−0.53	−3.33	−3.86	234

At low temperatures, strain accumulation exhibits a strong geometry dependence. At T = 100 K and P = 0 MPa, the total strain is approximately −2.2×10⁻⁴ for planar structures and −3.8×10⁻⁴ for radial structures. Under P = 200 MPa at T = 10 K, the total strain increases to −2.3×10⁻³ (planar) and −3.8×10⁻³ (radial), indicating that radial strain is ~1.7×higher

than planar at low temperature. This clearly shows that pressure-induced strain dominates over thermal effects at P > 100 MPa. For planar geometries, the thermal expansion mismatch between GaAs ($\alpha = 5.8\times10^{-6}$ K^{-1}) and Si ($\alpha = 2.6\times10^{-6}$ K^{-1}) results in significant in-plane thermal stress. At T = 300 K (reference), the strain is ~0, whereas at T = 10 K and P = 0 MPa, the total thermal strain reaches $\varepsilon \approx (5.8 - 2.6)\times10^{-6}\times(10 - 300) \approx -8.0\times10^{-4}$. When pressure is increased to P = 200 MPa, the total strain exceeds -2.8×10^{-3}, producing high compressive stress that can drive crack formation or dislocation generation at the heterointerface. Surface plot contours reveal a strong nonlinear dependence of total strain on both temperature and pressure. In contrast, radial structures exhibit reduced effective thermal expansion due to radial compliance and a lower elastic modulus (E = 60 GPa). At T = 10 K and P = 0 MPa, the thermal strain is $\varepsilon \approx -5.3\times10^{-4}$, while at P = 200 MPa, the total strain reaches -3.9×10^{-3}. Although the magnitude of total strain is larger in radial structures, the resulting mechanical stress remains lower because of the smaller elastic modulus: $\sigma_{radial} \approx 60\ \text{GPa} \times 3.9 \times 10^{-3} \approx 234$ MPa, $\sigma_{planar} \approx 100\ \text{GPa} \times 2.8 \times 10^{-3} \approx 280$ MPa. This confirms that radial designs accommodate strain more efficiently, reducing stress concentrations and enhancing interface stability. Thermal strain amplitude: Planar ≈ 8.0×10^{-4}; Radial ≈ 5.3×10^{-4}. Pressure strain amplitude (200 MPa): Planar ≈ 2.0×10^{-3}; Radial ≈ 3.33×10^{-3}. Maximum stress: Planar ≈ 280 MPa; Radial ≈ 234 MPa. Thermal mismatch strain reduction in radial design: ≈ 34 %. These results demonstrate that radial heterojunction architectures provide superior strain accommodation and stress relaxation, significantly mitigating the risks of delamination, interface cracking, and performance degradation. This mechanical advantage is particularly valuable for high-power optoelectronic and photovoltaic devices, where long-term structural integrity under thermal–mechanical loading is critical.

CONCLUSIONS

This work provides a comprehensive analysis of thermal, electronic, and mechanical effects in planar and radial Si/GaAs p–n junctions under varying temperature (10–300 K) and pressure (0–200 MPa). The results demonstrate that radial heterojunctions, with ~2D strain distribution, allow greater thermal expansion freedom (0.17 % for GaAs vs. 0.078 % for Si), leading to a 34 % reduction in thermal mismatch strain and a stress drop from 280 MPa (planar) to 234 MPa (radial). Thermal bandgap narrowing was accurately modeled using Varshni and Pässler relations, showing that Eg(GaAs) decreases from 1.519 eV (0 K) to 1.4078 eV (300 K) and Eg(Si) from 1.170 eV to 1.0823 eV. The bandgap difference shrinks from 0.349 eV at 0 K to 0.298 eV (Varshni) and 0.325 eV (Pässler) at 300 K. These temperature effects are critical for heterostructure band alignment and optoelectronic device efficiency. Mechanically, radial architectures accommodate 1.7× higher strain at cryogenic temperatures but generate lower stress levels due to reduced stiffness (E = 60 GPa), suppressing defect formation such as misfit dislocations. This structural advantage enables enhanced reliability and performance of photodetectors, LEDs, and solar cells under extreme thermal–mechanical loading. Overall, this study confirms that radial p–n junctions outperform planar designs, offering improved thermal stability, mechanical tolerance, and electronic performance making them a promising platform for next-generation optoelectronic and energy devices.

ORCID

Jonibek Sh. Abdullayev, https://orcid.org/0000-0001-8950-2135
Madinabonu Sh. Ibragimova, https://orcid.org/0009-0004-7867-7086
Jo'shqin Sh. Abdullayev, https://orcid.org/0000-0001-6110-6616
Ibrokhim B. Sapaev, https://orcid.org/0000-0003-2365-1554

REFERENCES

[1] K.K.D. Nigam, P. Yadav, *et al.*, "Numerical Investigation of $RbGeI_3$-Based Lead-Free Perovskite Solar Cell with Various Cu-Based Hole Transport Layers Using SCAPS-1D," J. Electron. Mater. **54**, 2747–2765 (2025). https://doi.org/10.1007/s11664-025-11740-x

[2] G.S. Sahoo, C. Harini, N. Mahadevi, P.S. Nethra, A. Tripathy, M. Verma, and G.P. Mishra, "CuO film as recombination blocking layer in Si solar cells," Silicon, **15**, 4039–4048 (2023). https://doi.org/10.1007/s12633-023-02701-x

[3] Lepkowski, D. L., Garassman, T. J., Boyer, J. T., Chmielewski, D. J., Yi, C., Juhl, M. K., Ringel, S. A. (2021). 23.4% monolithic epitaxial GaAsP/Si tandem solar cell. Solar Energy Materials and Solar Cells, 230, 111299. https://doi.org/10.1016/j.solmat.2021.111299

[4] S. Fan, Z.J. Yu, Y. Sun, W. Weigand, P. Dhingra, M. Kim, *et al*., "20%-efficient epitaxial GaAsP/Si tandem solar cells," Solar Energy Materials and Solar Cells, **202**, 110144 (2019). https://doi.org/10.1016/j.solmat.2019.110144

[5] A. Qu, Z. Xie, Y. Wang, *et al.* "Effect of Acceptor-Type Traps in GaN Buffer Layer on Current Collapse of ε-Ga_2O_3/GaN HEMTs," J. Electron. Mater. **54**, 3086–3096 (2025). https://doi.org/10.1007/s11664-025-11823-9

[6] J.Sh. Abdullayev, I.B. Sapaev, J.Sh. Abdullayev, D.A. Juraev, M.J. Jalalov, E.E. Elsayed, "Mathematical modeling of incomplete ionization in radial p-Si/n-GaAs heterojunctions: temperature and doping effects", Journal of Electronic Materials, **54**, 10484-10492 (2025). https://doi.org/10.1007/s11664-025-12391-8

[7] Li, D., Luo, C., Wang, H., Ling, F., and Yao, J. (2021). Active control of plasmon-induced transparency based on a GaAs/Si heterojunction in the terahertz range. Optical Materials, 114, 111609. https://doi.org/10.1016/j.optmat.2021.111609

[8] J.S. Abdullayev, D.A. Qalandarova, M.S. Ibragimova, *et al*. "Experimental and Simulation-Based Investigation of p-Si/n-CdS Heterojunctions: From Cryogenic Freeze-Out to Room Temperature Operation," Journal of Electronic Materials, **55**, 2229–2239 (2026).https://doi.org/10.1007/s11664-025-12642-8

[9] Hasan, M.N., Zheng, Y., Lai, J., Swinnich, E., Licata, O.G., Baboli, M.A., Mazumder, B., Mohseni, P.K., and Seo, J.-H. "Influences of native oxide on the properties of ultrathin Al_2O_3-interfaced Si/GaAs heterojunctions," Advanced Materials Interfaces, **9**(13), 2101531 (2022). https://doi.org/10.1002/admi.202101531

[10] I.B. Sapaev, J.I. Razzokov, J.S. Abdullayev, D.A. Qalandarova, and M.S. Ibragimova, "Bandgap-Engineered pSi/n-Cd_xS_{1-x} Heterojunctions: Effect of Composition on Optoelectronic Behavior," East European Journal of Physics, (4), 442-448 (2025).https://doi.org/10.26565/2312-4334-2025-4-44
[11] Jurisch, M., Börner, F., Bünger, T., Eichler, S., Flade, T., Kretzer, U., Köhler, A., Stenzenberger, J., and Weinert, B. (2005). LEC- and VGF-growth of SI GaAs single crystals—Recent developments and current issues. Journal of Crystal Growth, 275(1–2), 283–291. https://doi.org/10.1016/j.jcrysgro.2004.10.092
[12] Abdullayev, J. Sh., Sapaev, I. B., and Juraev, Kh. N. (2025). Theoretical analysis of incomplete ionization on the electrical behavior of radial p-n junction structures. Low Temperature Physics, 51, 60–64. https://doi.org/10.1063/10.0034646
[13] Garg, P. Design and Optimization of a Metamaterial Absorber Using Machine Learning Models. *J. Electron. Mater.* **55**, 790–799 (2026). https://doi.org/10.1007/s11664-025-12516-z
[14] Abdullayev, J. Sh., and Sapaev, I. B. (2024). Factors influencing the ideality factor of semiconductor p-n and p-i-n junction structures at cryogenic temperatures. East European Journal of Physics, 4, 329–333. https://doi.org/10.26565/2312-4334-2024-4-37
[15] Thurmond, C. D. (1975). The standard thermodynamic functions for the formation of electrons and holes in Ge, Si, GaAs, and GaP. Journal of The Electrochemical Society, 122(8), 1133. https://doi.org/10.1149/1.2134410
[16] Herfort, J., Schönherr, H.-P., and Ploog, K. H. (2003). Epitaxial growth of hybrid structures. Applied Physics Letters, 83(18), 3912–3914. https://doi.org/10.1063/1.1625426
[17] Bharti, Mittal, P. Core–Shell Incorporated Analytical Modeling of a Dual-Material Gate Junctionless Nanowire: Extraction of Subthreshold Characteristics. *J. Electron. Mater.* **54**, 3046–3059 (2025). https://doi.org/10.1007/s11664-025-11737-6
[18] Bhardwaj, A., Das, A., Garg, P. *et al.* Material-Driven Performance Analysis of a Vertical Nanowire Tunnel FET for Analog Applications. *J. Electron. Mater.* **55**, 1099–1110 (2026). https://doi.org/10.1007/s11664-025-12438-w
[19] Abdullayev, J. Sh. (2025). Influence of linear doping profiles on the electrophysical features of p-n junctions. East European Journal of Physics, 1, 245–249. https://doi.org/10.26565/2312-4334-2025-1-26
[20] Heun, S., Sugiyama, M., Maeyama, S., Watanabe, Y., Wada, K., and Oshima, M. (1996). Growth of Si on different GaAs surfaces: A comparative study. Physical Review B, 53, 13534–13541. https://doi.org/10.1103/PhysRevB.53.13534
[21] Saxena, P. K., Srivastava, P., and Srivastava, A. (2024). Defect analysis of MBE reactor-grown HgCdTe on Si, GaAs, GaSb, and CZT substrates through the TNL-Epigrow simulator. Journal of Electronic Materials, 53, 5803–5812. https://doi.org/10.1007/s11664-024-11082-0
[22] Bardhan Roy, A., Rasulji Valiji, N. H., Mohammad, R., Giridhar, P., and Mondal, P. (2024). Performance enhancement of Si/GaAs based heterojunction solar cells by opto-electronics modeling and optimization. In 2024 International Conference on Recent Advances in Electrical, Electronics, Ubiquitous Communication, and Computational Intelligence (RAEEUCCI) (pp. 1–6). IEEE. https://doi.org/10.1109/RAEEUCCI61380.2024.10547792
[23] Abdullayev, J. Sh., and Sapaev, I. B. (2025). Analytic analysis of the features of GaAs/Si radial heterojunctions: Influence of temperature and concentration. East European Journal of Physics, 1, 204–210. https://doi.org/10.26565/2312-4334-2025-1-21
[24] Piriyev, M., Loget, G., Léger, Y., Chen, L., Létoublon, A., Rohel, T., Levallois, C., Le Pouliquen, J., Fabre, B., Bertru, N., and Cornet, C. (2023). Dual bandgap operation of a GaAs/Si photoelectrode. Solar Energy Materials and Solar Cells, 251, 112138. https://doi.org/10.1016/j.solmat.2022.112138
[25] Alanis, J., Gutiérrez-Ojeda, S. J., Méndez-Camacho, R., and Cruz-Hernández, E. (2024). Theoretical investigation of the growth of GaAs on Si(001), Si(110), Si(111), Si(113), and Si(331). Surfaces and Interfaces, 44, 103792. https://doi.org/10.1016/j.surfin.2023.103792
[26] Cao, S.D., Sai, D.C., Ngac, A.B. *et al.* Studies on the Impact of the Core-Shell Structures on the Optical Characteristics of Au@Cu_2O Nanoparticles. *J. Electron. Mater.* (2026). https://doi.org/10.1007/s11664-026-12690-8
[27] B. Abdullaev, and D. Qalandarova, "The classes of $(A)sh_m$ and $(B)sh_m$ functions," Annales Polonici Mathematici, **132**, 101-108 (2024).https://doi.org/10.4064/ap230727-30-11
[28] Huang, R., Wang, Q., Guo, Y., and Wang, Z. (2023). Comparative study on GaAs/Si heterojunction fabricated by nitrogen and oxygen plasma activated bonding. Vacuum, 208, 111735. https://doi.org/10.1016/j.vacuum.2022.111735
[29] Yamaguchi, M., Takamoto, T., Juso, H., Nakamura, K., Ozaki, R., and Kojima, N. (2024). 33.7% efficiency Si tandem solar cell modules. In Proceedings of the 2024 IEEE 52nd Photovoltaic Specialist Conference (PVSC). IEEE. https://doi.org/10.1109/PVSC57443.2024.10749502
[30] Šagátová, A., Novák, A., Kováčová, E., Riabukhin, O., Kotorová, S., and Zaťko, B. (2023). Radiation-degraded Si GaAs detectors and their metallization. AIP Conference Proceedings, 2778, 060009. https://doi.org/10.1063/5.0137383
[31] Liang, J., Chai, L., Nishida, S., Morimoto, M., and Shigekawa, N. (2015). Investigation on the interface resistance of Si/GaAs heterojunctions fabricated by surface-activated bonding. Japanese Journal of Applied Physics, 54(3), 030211. https://doi.org/10.7567/JJAP.54.030211
[32] Prasad, R.K., Singh, D.K. Melamine-Based Graphitic C_3N_4/p-Silicon Heterostructure Photodetector: Effect of g-C_3N_4 Growth Time on Performance. *J. Electron. Mater.* **54**, 3014–3023 (2025). https://doi.org/10.1007/s11664-025-11782-1
[33] Haris, M., Loan, S. A., and Mainuddin. (2019). Si/GaAs hetero junction tunnel FET: Design and investigation. Journal of Nanoelectronics and Optoelectronics, 14(10), 1434–1444. https://doi.org/10.1166/jno.2019.2575
[34] Liang, J., Miyazaki, T., Morimoto, M., Nishida, S., Watanabe, N., and Shigekawa, N. (2013). Electrical properties of p-Si/n-GaAs heterojunctions by using surface-activated bonding. Applied Physics Express, 6(2), 021801. https://doi.org/10.7567/APEX.6.021801
[35] Strzelecka, S., Pawlowska, M., Hruban, A., Gladysz, M., Wegner, E., Gladki, A., and Orlowski, W. (1997). Investigation of As-precipitates in SI GaAs. In J. Zmija, A. Majchrowski, J. Rutkowski, and J. Zielinski (Eds.), Solid State Crystals: Growth and Characterization (Vol. 3178, pp. 238–241). SPIE. https://doi.org/10.1117/12.280741
[36] Yu, T., Zhang, H., Li, D., and Lu, Y. (2021). Electronic and optical properties of silicene on GaAs(111) with hydrogen intercalation: A first-principles study. RSC Advances, 11, 16040–16050. https://doi.org/10.1039/D1RA01959G

[37] Sushkov, A. A., Pavlov, D. A., Andrianov, A. I., Shengurov, V. G., Denisov, S. A., Chalkov, V. Y., Kriukov, R. N., Baidus, N. V., Yurasov, D. V., and Rykov, A. V. (2022). Comparison of III–V heterostructures grown on Ge/Si, Ge/SOI, and GaAs. Semiconductors, 56, 122–133. https://doi.org/10.1134/S106378262201012X
[38] Huang, R., Wang, Z., Wu, K., Xu, H., Wang, Q., and Guo, Y. (2024). Hybrid bonding of GaAs and Si wafers at low temperature by Ar plasma activation. Journal of Semiconductors, 45(4), 042701. https://doi.org/10.1088/1674-4926/45/4/042701
[39] Lourenço, S. A., Dias, I. F. L., Duarte, J. L., Laureto, E., Poças, L. C., Toginho Filho, D. O., and Leite, J. R. (2004). Thermal expansion contribution to the temperature dependence of excitonic transitions in GaAs and AlGaAs. Brazilian Journal of Physics, 34(2a). https://doi.org/10.1590/S0103-97332004000300031
[40] Pässler, R. (2001). Basic model relations for temperature dependencies of fundamental energy gaps in semiconductors. Physica Status Solidi (b), *200*(1), 155–172. https://doi.org/10.1002/1521-3951(199703)200:1<155::AID-PSSB155>3.0.CO;2-3
[41] Jahromi, H. D., Zeiri, N., and Lotfiani, A. (2025). CMOS-integrated UV phototransistor utilizing a novel p-GaAs/p-Si staggered heterojunction. Journal of Science: Advanced Materials and Devices, **10**(3), 100891. https://doi.org/10.1016/j.jsamd.2025.100891
[42] Mishra, P.K., Maity, G. Impact of Oxygen Vacancies on Photodetection Performance of Ga_2O_3: A Comprehensive Review. J. Electron. Mater. **54**, 2533–2545 (2025). https://doi.org/10.1007/s11664-025-11746-5

ХАРАКТЕРИСТИКИ ТЕПЛОВОГО РОЗШИРЕННЯ ПЛОСКИХ ТА РАДІАЛЬНИХ ГЕТЕРОПЕРЕХОДІВ p–n Si/GaAs

Джонібек Ш. Абдуллаєв[1], Мадінабону Ш. Ібрагімова[1], Джошкін Ш. Абдуллаєв[2], Іброхім Б. Сапаєв[2,3,4,5]
[1]Ургенчський державний університет, вулиця Хаміда Олімджона, 14, Ургенч, 220100, Узбекистан
[2]Національний дослідницький університет ТІІАМЕ, кафедра фізики та хімії, Ташкент, Узбекистан
[3]Західно-Каспійський університет, Баку, Азербайджан
[4]Ташкентський університет прикладних наук, вулиця Університетська, 28, Ташкент 100095, Узбекистан
[5]Інженерний факультет, Центральноазіатський університет, Ташкент 111221, Узбекистан

У цій роботі представлено комплексне теоретичне та чисельне дослідження плоских та радіальних p–n гетеропереходів Si/GaAs, зосереджене на спільному впливі термічного розширення та неповної іонізації домішок на електростатичні та механічні характеристики структур. Двовимірне рівняння Пуассона розв'язано в декартовій та циліндричній системах координат з урахуванням імовірнісної активації домішок для моделювання заморожування носіїв при низьких температурах. При 100 K неповна іонізація зменшує вбудований потенціал на до 40 % і збільшує ширину збідненої області більш ніж на 50 %, тоді як радіальні переходи демонструють на 15–25 % вищий потенціал завдяки криволінійному посиленню поля. Термомеханічне моделювання показало, що при 10 K та тиску 200 МПа у плоских структурах загальна деформація досягає $-2{,}8 \times 10^{-3}$, а напруження — ≈280 МПа, тоді як у радіальних структурах спостерігається деформація $-3{,}9 \times 10^{-3}$, але менше напруження (≈234 МПа) через знижений модуль пружності. Отримані результати демонструють переваги радіальної геометрії щодо релаксації напружень та підвищення електростатичного контролю, що є важливим для високоефективних кріогенних фотодетекторів та оптоелектронних пристроїв.

Ключові слова: *радіальний p–n перехід; плоский p–n перехід; неповна іонізація; термічне розширення; циліндрична система координат; декартова система координат; низькотемпературні ефекти*